Numerical Simulation of HiPEP Ion Optics

Cody C. Farnell*
Colorado State University

The ffx code was used to investigate the lifetime and propellant throughput capability of the High Power Electric Propulsion (HiPEP) thruster ion optics as part of NASA's Project Prometheus. Erosion predictions are presented as a function of beamlet current, accel grid voltage, and propellant utilization efficiency. These predictions were then compared to the lifetime goals of the thruster, and for nominal operating conditions, the ffx code indicates that the HiPEP thruster will have propellant throughput capability of 100 kg/kW and lifetimes in excess of 135 khrs. In addition to lifetime assessment, a detailed study was completed where grid design parameters were varied in a systematic manner to determine their effects on beamlet current limitations and electron backstreaming margins. The parameters that were varied included the net and total accelerating voltage, grid spacing, aperture center-to-center distance, accel grid thickness, screen grid thickness, discharge voltage, and accel grid aperture diameter.

INTRODUCTION

The High Power Electric Propulsion (HiPEP) thruster is being developed at NASA Glenn as a possible candidate for future use with space systems under Project Prometheus.[1] The thruster is being designed to operate at approximately 25 kW of power and have a propellant throughput capability of about 100 kg per kW of power. The thruster will operate using xenon as the propellant and have specific impulse values in the range of 6000 to 9000 seconds. To reach its propellant throughput goal, the thruster will operate for many years (10 to 15) using long lasting carbon grids. One assembly that may lead to the eventual failure of the thruster is the ion optics system. With such a large thruster lifetime, the possibility of demonstrating life experimentally is not feasible and numerical or analytical approaches must be used instead. A numerical simulation code called ffx has been under development at Colorado State University for the past two years, and this paper presents a lifetime assessment of the HiPEP optics system using this code. The first section of the paper contains details of the HiPEP geometry and operating conditions. The second section contains a brief description of the ffx code. This section is followed by a discussion of beamlet current limitations and electron backstreaming margins and how they are simulated using ffx. Finally, the results section is split up into two subsections that present (1) crossover, perveance, and backstreaming limits and (2) grid erosion predictions.

GRID SET GEOMETRY & OPERATING CONDITIONS

The HiPEP thruster will use a two-grid ion optics system. The nominal grid geometry and operating conditions used in this paper are listed in Table 1. This information is closely representative of the HiPEP design for high specific impulse operation. However, some values in this table are subject to variation as the HiPEP thruster goes through developmental progressions. The total beam current, J_B, of 3.5 A and net accelerating voltage, V_N, of 6700 V indicate a thruster power, P, near 25 kW. The number of holes in the grid set was calculated from the hole center-to-center spacing, ℓ_{cc}, and the total beam area, A_B. Beamlet current, J_b, is the amount of ion current going through a single aperture pair in the grid set. The thruster beam current was divided by the number of holes to obtain the average beamlet current, $J_{b\ avg}$. The value of the flatness parameter, F, was varied in the current study from a value of 0.6 to a value of 0.8. The peak beamlet current, $J_{b\ peak}$, listed in this table was calculated using a flatness parameter of 0.7.

* Graduate Research Assistant, AIAA Student Member, 1320 Campus Delivery, Fort Collins, CO 80523

Table 1. Standard HiPEP grid geometry and operating conditions.

Geometry

Parameter	Symbol	Units	Value
Screen Grid Thickness	t_s	mm/mm	3.94
Screen Grid Diameter	d_s	mm/mm	5.25
Grid Spacing	ℓ_g	mm/mm	9.09
Accel Grid Thickness	t_a	mm/mm	3.94
Accel Grid Diameter	d_a	mm/mm	5.25
Aperture Center-To-Center Spacing	ℓ_{cc}	mm/mm	5.20
Beam Area	A_B	cm^2	3690
Holes	-	-	3222

Operating Conditions

Parameter	Symbol	Units	Value
Beam Current	J_B	A	3.5
Net Accelerating Voltage	V_N	V	6700
Discharge Voltage	V_d	V	26
Accel Grid Voltage	V_a	V	-650
Power	P	kW	~ 25
Flatness Parameter	F	-	~ 0.7
Average Beamlet Current	$J_{b\,avg}$	mA	1.09
Peak Beamlet Current	$J_{b\,peak}$	mA	1.55
Propellant Utilization Efficiency	η_u	-	~ 0.92

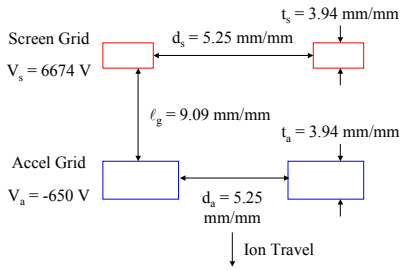

Fig. 1 Layout of HiPEP geometry.

DESCRIPTION OF THE "ffx" CODE

The ffx code is a three-dimensional ion optics code. The simulation domain is rectangular, and for a hexagonal grid aperture layout, there are two quarter sized holes located at opposite corners of the region. Figure 2 shows the three dimensional ffx code simulation region for the standard grid geometry. This figure shows how the symmetry conditions that are imposed on four sides of a single analysis region can be used to construct a full aperture pair. A typical simulation mesh size is 32 x-cells by 56 y-cells by 300 z-cells. A combination of the multigrid method and successive over-relaxation are used to solve Poisson's equation for mesh potential values. Approximately 15,000 ion macro particles are sent through the domain on each iteration to obtain ion and electron space charge as a function of the specified beamlet current. Normal ion incidence sputter yields are calculated using data from Yamamura and Tawara[2] and are adjusted according to an angular dependency for xenon on molybdenum. Further information regarding the methods used in the ffx code can be found in Farnell et al.[3]

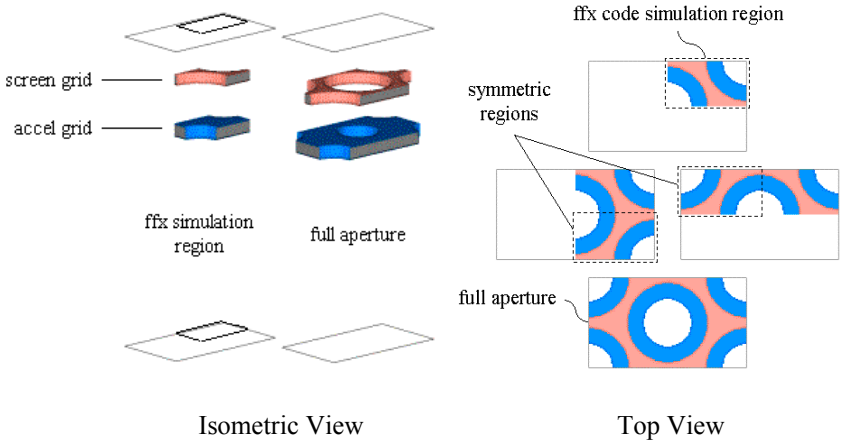

Fig. 2 The ffx code simulation region. The symmetry conditions that exist on four sides of the region are used to construct a picture of the full aperture pair.

IMPINGEMENT LIMITS

For each grid geometry and operating voltage, a curve of accel grid impingement current, J_a, versus beamlet current, J_b, can be obtained. The accel grid impingement current can be divided by the beamlet current and then plotted versus beamlet current to obtain what will be referred to as an impingement limit curve. The impingement limit curve for the standard geometry and voltages (V_N = 6700 V, V_a = -650 V) is shown in Fig. 3. In this curve, the flow rate was set to a constant value, 3.0 mA equivalent per hole, as is normally done in experimental gridlet testing performed at CSU. Thus, the propellant utilization efficiency decreases as beamlet current decreases. Both charge exchange and directly impinging beam (i.e., non-charge exchange) ions can be collected on the accelerator grid. The charge exchange ion current is unavoidable, but operational conditions exist where directly impinging beam ions can be avoided.

The two values obtained from an impingement limit curve are the crossover and perveance limits. The crossover limit is defined as the beamlet current where beam ions are accelerated across the beamlet centerline and begin to impinge upon the accel grid barrel on the opposite side of the aperture from which they started. The perveance limit is defined as the beamlet current where beam ions are accelerated nearly directly downstream and begin to impinge upon the upstream side of the accel grid (or the accel grid barrel). Figure 4 shows the shape of the ion beamlet for three beamlet currents, one at the crossover limit (0.30 mA), one at the perveance limit (2.55 mA), and one at a current between the two limits (1.40 mA). Erosion caused by ions originating from the discharge chamber can be significant, as these ions strike the accel grid with very high energy. For this reason, it is desirable to operate all apertures on the thruster grid set between the crossover and perveance limit beamlet currents.

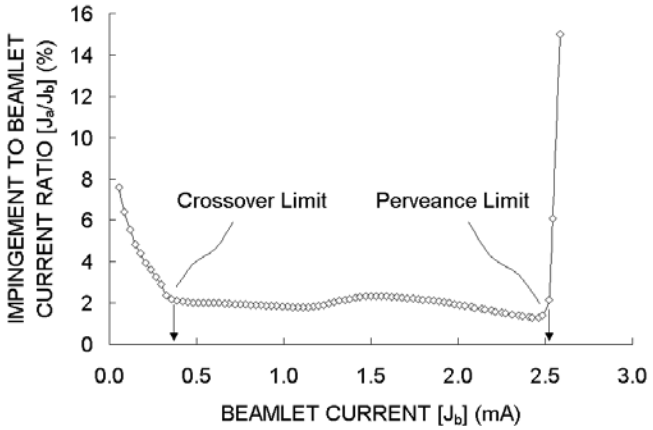

Fig. 3 Impingement limit curve for the standard geometry and operating voltages.

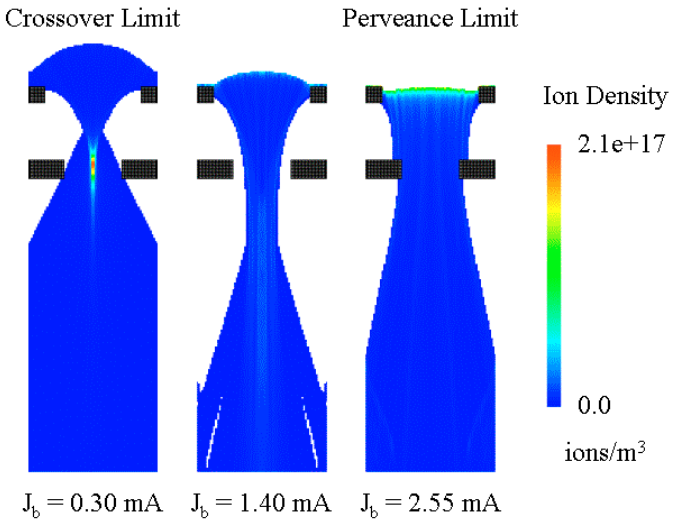

Fig. 4 Ion beamlet shape as a function of beamlet current for the standard grid geometry.

A parameter called normalized perveance per unit area[4] is defined in Eq. (1). This parameter can be used to determine the relative amount of ion extraction from an aperture compared to the theoretical maximum amount of ion extraction. There are several choices for the area, A, in this equation depending upon the goal of the calculation. One choice is the open area per hole, A_h, which in this study is defined using the cross-sectional area of the screen grid hole, and the other is the total area per hole, A_g, which includes the open area of the screen grid hole as well as the associated grid area between holes. Using the open area per hole gives P_h, the normalized perveance per unit hole area and using the total area per hole gives P_g, the normalized perveance per unit grid area.

$$P = \frac{J_b}{A}\frac{\ell_e^{\,2}}{V_T^{\,3/2}}\left(\frac{4\varepsilon_o}{9}\sqrt{\frac{2e}{m_i}}\right)^{-1}, \quad \text{where} \quad A_h = \frac{\pi d_s^{\,2}}{4} \qquad A_g = \frac{\sqrt{3}}{2}\ell_{cc}^{\,2} \tag{1}$$

$$\ell_e = \sqrt{\left(t_s + \ell_g\right)^2 + \frac{{d_s}^2}{4}} \tag{2}$$

In Eqs. (1) and (2), e represents the charge on a singly ionized ion, m_i the mass of a xenon ion, ε_o the permittivity of free space, and ℓ_e the effective acceleration length.

At the perveance limit, where the amount of ion extraction from a hole in a given geometry is at a maximum, the values of P_h and P_g will usually be less than unity. Equation (1) can be used to predict how the beamlet current at the perveance limit will vary as a function of the parameter listed (e.g., the total accelerating voltage, V_T, and grid spacing, ℓ_g). From this equation for example, the perveance limit is expected to increase as total voltage to the 3/2 power.

ELECTRON BACKSTREAMING

For each beamlet current, there is a point along the centerline of the ion beamlet that corresponds to the most negative potential. This value will be referred to as the centerline saddle point potential, V_{sp}, and it typically occurs near the exit plane of the accelerator grid. The saddle point potential can be used as an indicator of electron backstreaming in that more negative saddle point potentials will stop progressively more energetic beam plasma electrons from backstreaming through the accelerator grid aperture into the positively biased discharge plasma. A plot of the mesh potential values along the centerline of the ion beamlet is shown in Fig. 5 for a net voltage of 6700 V, an accel voltage of –750 V, and a beamlet current of 1.0 mA.

As the accel grid voltage magnitude is decreased, while holding the net accelerating voltage constant, the saddle point voltage will similarly increase, i.e. become less negative, to the point where electrons will likely be able to backstream from the downstream plasma to the discharge chamber plasma. The saddle point voltage at all beamlet currents can be plotted for a fixed accel grid voltage as shown in Fig. 6. From this figure, there is a typically a single beamlet current where the saddle point potential is the least negative and this point is therefore likely to correspond to the first location on a broad area source where electrons will backstream. The least negative accel grid voltage required to prevent electrons from backstreaming will be referred to as the backstreaming voltage. The shape of the curve in Fig. 6 tends to remain the same as accel grid voltage is decreased. The margin against backstreaming is the voltage difference of the operating accel grid voltage and the backstreaming limit voltage. For instance, if the operating accel grid voltage is –650 V and electron backstreaming starts to occur in earnest when the applied accel grid voltage is –620 V, the margin against electron backstreaming is 30 V.

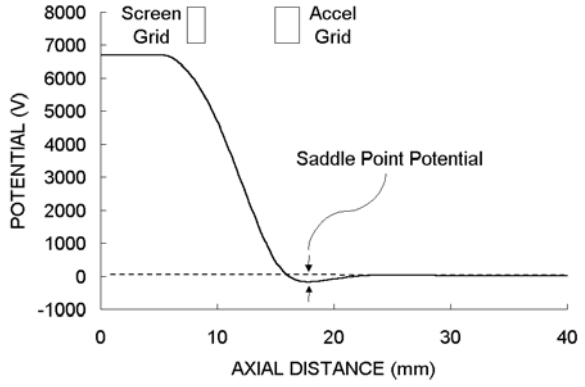

Fig. 5 Potential values along the centerline of an ion beamlet operating at a beamlet current of 1.0 mA and the standard grid voltages.

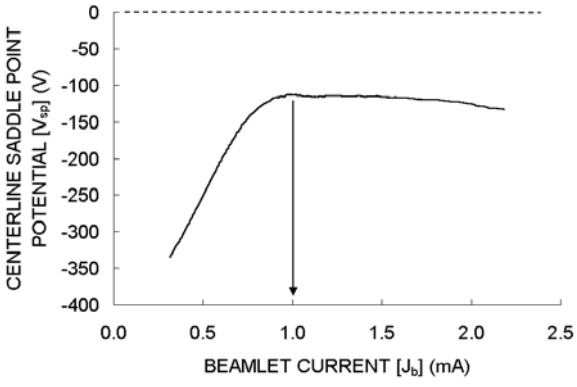

Fig. 6 Saddle point potential as a function of beamlet current for the standard grid set geometry and operating voltages.

RESULTS

The results section is divided into two subsections. The first subsection discusses the impingement and backstreaming limits calculated using ffx and presents sensitivity measurements of these limits on HiPEP geometry and operational conditions. The second subsection contains results of life time assessments.

CROSSOVER, PERVEANCE, & BACKSTREAMING LIMITS

One of the main goals of this study is to determine the sensitivity of the grid design to changes in individual parameters. In this paper, the sensitivity of the standard grid design to changes in total voltage (V_T), accel grid voltage (V_a), grid spacing (ℓ_g), aperture center-to-center spacing (ℓ_{cc}), accel grid thickness (t_a), screen grid thickness (t_s), discharge voltage (V_d), and accel grid hole diameter (d_a) are reported.

The ffx code was first used to determine how the crossover and perveance limits changed as a function of total voltage, the results of which are shown in Fig. 7. The ratio of the net to total accelerating voltage is called the R value and is defined in Eq. (3). The R value in the standard case, where the net voltage is 6700 V and the accel voltage is –650V, is 0.912. As total voltage was varied, the R value was kept constant such that the standard R value was used to set the accel grid voltage at each total voltage case. Also shown in Fig. 7 are the average and peak beamlet currents at each total voltage value that are calculated in keeping a constant thruster power level near 25 kW. As total voltage decreases for example, the beam current must increase for the same thruster power. Below a total voltage of about 6000 V, the peak beamlet current is greater than the perveance limit and one would expect ions to be directly impinging upon the accel grid if the power is not reduced.

$$R = \frac{V_N}{V_T} = \frac{V_N}{V_N + |V_a|} \quad \text{or} \quad |V_A| = V_N\left(\frac{1-R}{R}\right) \tag{3}$$

As mentioned before, the perveance limit is expected to vary as total voltage to the 3/2 power. The sensitivity of the grid design to total voltage, as found using the ffx code, can be calculated by normalizing the beamlet currents and total voltages in Fig. 7 by the standard total voltage or impingement limit value. See Williams et al.[5] for a more detailed description of this procedure. The result of this operation on total voltage is shown in Fig. 8. The slope of a linear curve fit through the normalized crossover or perveance limit curve is the sensitivity value. In this case, the sensitivity of the perveance limit to total voltage was found to be 1.49, which is close to the equation prediction of 1.50. For the standard case, where the total voltage is 7350 V, the value of normalized perveance per unit hole area, P_h, at the perveance limit was 0.84. The sensitivity of the crossover limit to total voltage was 1.94. Experimental total voltage sensitivities from Williams et al.[5], which were determined using grid geometries and voltages close to the standard values listed in Table 1, for the crossover and perveance limits were 1.42 and 1.55 respectively.

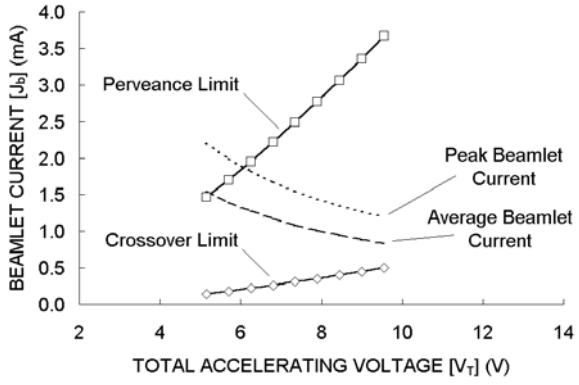

Fig. 7 Effect of net accelerating voltage (V_N) on the perveance and crossover limits.

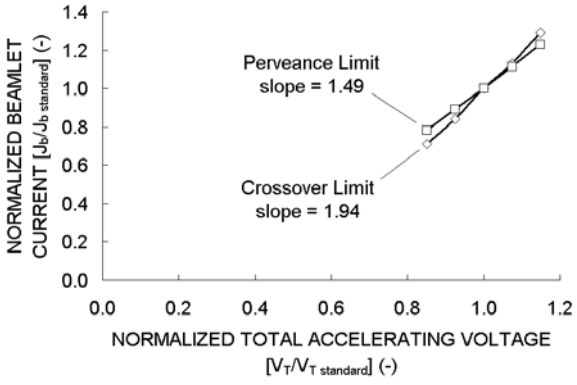

Fig. 8 Normalized crossover and perveance limits as a function of normalized total accelerating voltage.

A study was done at a constant net accelerating voltage of 6700 V with varying accel grid voltage to see how the crossover limit, perveance limit, and saddle point potential changed as a function of accel grid voltage. The crossover and perveance limits at different accel grid voltages should vary in a manner similar to when total accelerating voltage is varied. In this simulation case, the net voltage, rather than the R value, was fixed as the total voltage was changed. Figure 9 shows how the crossover and perveance limits change as the accel grid voltage is varied from –650 to –1050 V. The sensitivities of the crossover and perveance limits to accel grid voltage were 0.18 and 0.14, respectively, and the sensitivities of the crossover and perveance limits to total voltage were 2.02 and 1.53 respectively. From before, where total voltage was changed with constant R value, the sensitivities of the crossover and perveance limits to total voltage were 1.94 and 1.49, respectively. Similar sensitivities are thus observed in both the constant net voltage and R value cases.

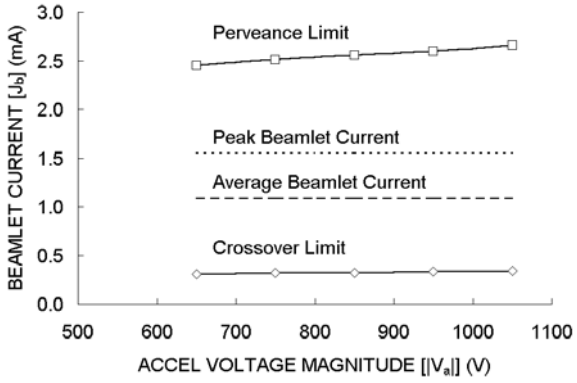

Fig. 9 Crossover and perveance limits as a function of accel grid voltage magnitude at a net voltage of 6700 V.

The centerline saddle point potential as a function of beamlet current was seen to vary linearly with accel grid voltage as shown in Fig. 10. At each accel grid voltage, the least negative saddle point potential occurs at a beamlet current between 0.5 and 1.0 mA. These "maximum" saddle point voltages are taken from Fig. 10 and plotted in Fig. 11 as a function of accel grid voltage magnitude. From this figure, it is seen that with each 100 V decrease in the accel grid voltage magnitude, the centerline saddle point potential becomes less negative by 85.3 V. Although it is noted that this relationship between accel grid voltage and the saddle point potential could be different for other grid geometries and net accelerating voltages, the relationship can be used to predict the backstreaming limit voltage, which is the accel grid voltage at which electron backstreaming will occur, given the saddle point potential at a certain accel grid voltage.

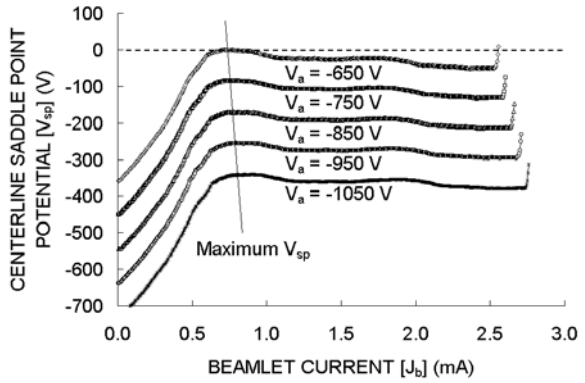

Fig. 10 Saddle point potential as a function of beamlet current and accel grid voltage.

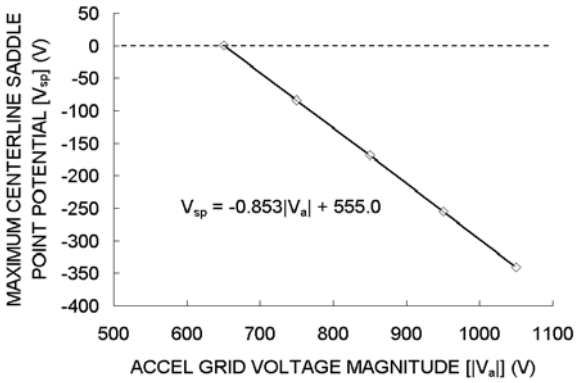

Fig. 11 Maximum saddle point potentials as a function of accel grid voltage.

The next parameter studied was grid spacing, ℓ_g. The relationship between grid spacing and the effective grid spacing, ℓ_e, was given in equation (2). The effective grid spacing is a more accurate indicator of the length over which the ion acceleration takes place than grid spacing alone. Figure 12 shows how the perveance and crossover limits vary with effective grid spacing. In this figure, the five effective grid spacing values studied correspond to grid spacing values of 6.06, 7.57, 9.09 (standard), 10.60, and 12.11 mm/mm. Also shown in Fig. 12 are the average and peak beamlet currents calculated for a total beam current, J_B, of 3.5 A and 3222 holes with a flatness parameter, F, of 0.7. The average and peak beamlet currents should be between the perveance and crossover limits in order to

avoid ions from the discharge chamber directly impinging upon the accel grid. If a worst-case flatness parameter of 0.6 is used, the peak beamlet current is 1.81 mA, and at the 12.11 mm/mm grid spacing, this would be above the perveance limit.

From Eq. (1), the perveance limit should vary approximately as effective grid spacing to the -2 power. In plotting the normalized crossover and perveance limits versus normalized effective grid spacing, the data was nonlinear. Using all five data points, the sensitivities of the crossover and perveance limits to effective grid spacing were found to be –1.34 and –2.22 respectively. If instead only three data points are used surrounding the standard effective grid spacing of 6.39 mm/mm, the sensitivities of the crossover and perveance limits to effective grid spacing are –1.18 and –2.05 respectively. Thus, the perveance limit is predicted to behave in a manner that is close to the -2 power. Experimentally, again measured on slightly different grid geometry, the sensitivities of the crossover and perveance limits to effective grid spacing were –0.49 and –2.10.[5]

At the 9.09, 10.60, and 12.11 mm/mm grid spacings, an accel voltage of –650V is sufficient to suppress electron backstreaming, while greater accel grid voltages are needed at the 6.06 and 7.57 mm/mm grid spacings. The data in Fig. 12 were all calculated at an accel grid voltage of –850 V. Figure 13 shows how the backstreaming limit, i.e. the accel voltage required to prevent electron backstreaming, varies as a function of effective grid spacing. The data in this figure were obtained using curves similar to those in Fig. 10 combined with the relationship between saddle point voltage and accel grid voltage found from the accel grid voltage study discussed previously.

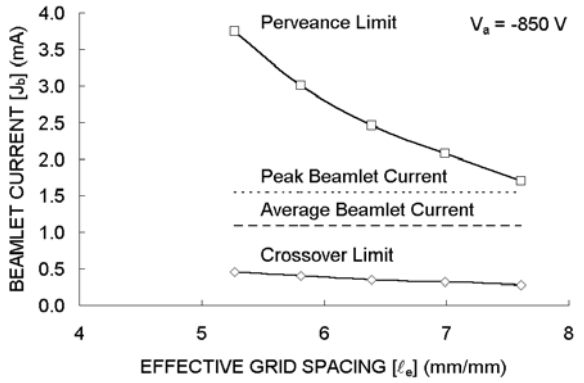

Fig. 12 Crossover and perveance limits as a function of effective grid spacing at a net voltage of 6700V.

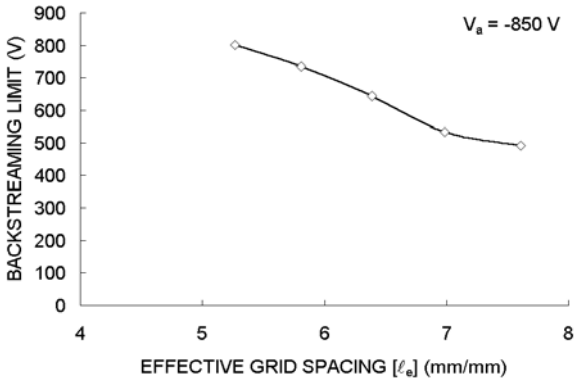

Fig. 13 Backstreaming limit as a function of grid spacing.

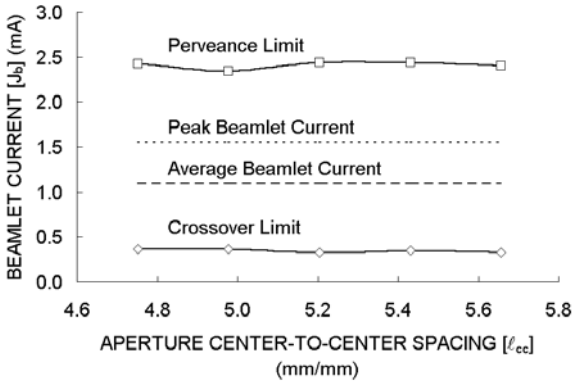

Fig. 14 Perveance and crossover limits as a function of aperture center-to-center spacing.

Figure 14 shows the effect of center-to-center spacing on the crossover and perveance limits. At low beamlet currents, the sheath that separates the discharge chamber plasma from the intra-grid region tends to move upstream. In some cases, interaction between several apertures can be seen in the sheath shape. This interaction can produce a six-sided "star-shaped" ion beamlet cross section. The level of interaction tends to increase with decreasing aperture center-to-center spacing and decreasing screen grid thickness.

The sensitivities of the crossover and perveance limits to aperture center-to-center spacing were –0.59 and 0.05 respectively. These sensitivities in particular have some uncertainty associated with them as the magnitude of the crossover and perveance limit changes were small and somewhat inconsistent as a function of center-to-center spacing. It was expected that the crossover limit would

increase as the center-to-center distance was decreased as a result of the star-shaped nature of the ion beamlet cross-section. The rate of rise of impingement current was seen to increase at the crossover limit as the aperture center-to-center distance was decreased due to the increasingly non-circular shape of the ion beamlet.

Figure 15 shows ion density cross sections of the ion beamlet taken at a plane even with the downstream side of the accel grid for three aperture center-to-center values at a beamlet current of 0.5 mA, which is near the crossover limit. The open area in this figure is that of the accel grid aperture, where the hole diameter stays constant at 5.25 mm/mm. The screen grid open area is larger and also held constant with a hole diameter of 5.25 mm/mm. It can be seen in this figure that the ion beamlet is definitely star shaped at the closest aperture center-to-center spacing. The diameter of the ion beamlet at the closest spacing appears to be only slightly greater than it is in the larger aperture center-to-center spacings. It is not surprising that the perveance limit does not change much with changing center-to-center spacing because at greater beamlet currents, the sheath is located further downstream and the sheaths from adjacent apertures do not interact as readily.

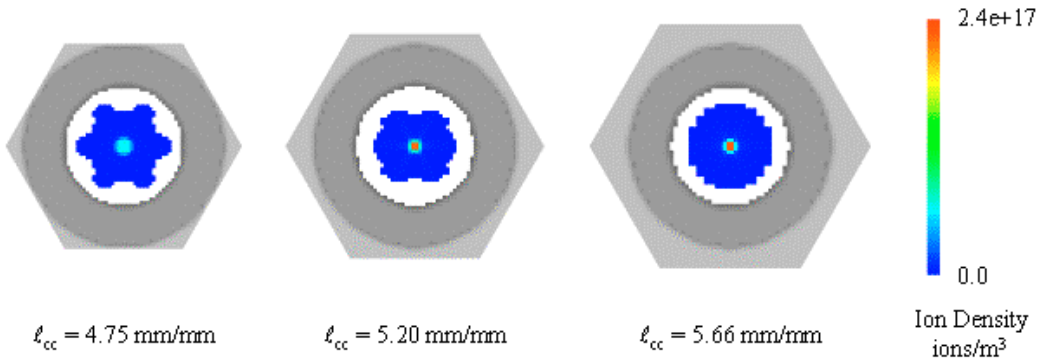

Fig. 15 Ion beamlet cross-sectional shape at the downstream side of the accel grid at a beamlet current of 0.5 mA.

One reason for decreasing the aperture center-to-center distance is to obtain a greater grid transparency to ions. Figure 16 shows how the grid transparency to ions changes as a function of aperture center-to-center distance at the average beamlet current of 1.09 mA. Similar trends in ion transparency as a function of center-to-center distance are seen at other beamlet currents. The difference between the ion and physical transparencies stays nearly constant at 5.5 % for all aperture center-to-center spacings at the 1.09 mA beamlet current.

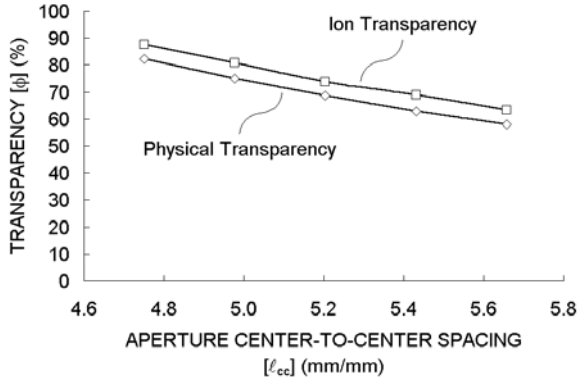

Fig. 16 Ion and physical grid transparencies at a beamlet current of 1.09 mA.

The crossover limit was found to depend more strongly on accel grid thickness than the perveance limit. Figure 17 shows the variation of the crossover and perveance limits with changing accel grid thickness. The data in this figure were all obtained at an accel grid voltage of –1050 V, as this was the voltage required to prevent electron backstreaming at the smallest accel grid thickness of 1.97 mm/mm. The resulting sensitivities of the crossover and perveance limits to accel grid thickness were 0.52 and –0.01 respectively. It was expected that the crossover limit would depend more strongly on accel grid thickness than the perveance limit.

In the perveance limit case, ions from the discharge chamber are accelerated nearly directly downstream and will often impinge on the upstream face of the accel grid before they will start to impinge on the accel grid barrel for the typical case where the accel grid hole diameter is

smaller than the screen grid hole diameter. For this reason, the accel grid hole diameter, for instance, is expected to affect the perveance limit more than accel grid thickness. In the crossover limit case, ions from the discharge chamber are accelerated from one side of the aperture across the beamlet centerline to an impingement point on the accel grid barrel on the other side of the aperture. The data, and intuition, indicate that as accel grid thickness was increased, ion impingement began at greater beamlet currents.

Figure 18 shows how the backstreaming limit varies with accel grid thickness. The data in this figure were estimated from the saddle point potential values found at an accel grid voltage of –1050 V along with the relationship between accel grid voltage and saddle point potential found previously. The variation in backstreaming limit with accel grid thickness can be important in cases where the accel grid is thinning due to erosion taking place on the downstream face of the accel grid.

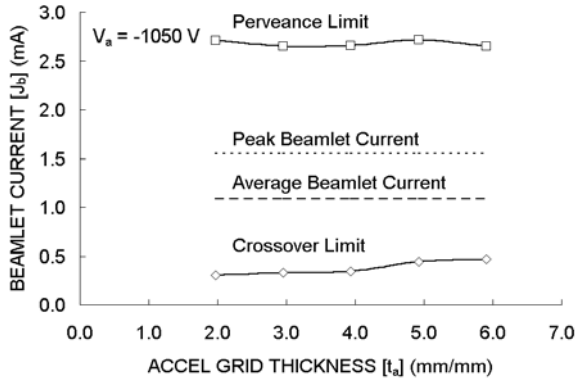

Fig. 17 Crossover and perveance limits as a function of accel grid thickness.

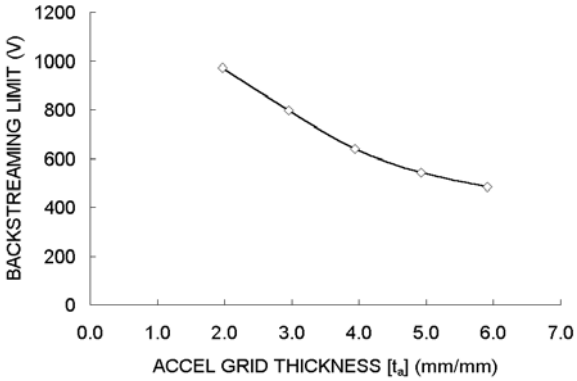

Fig. 18 Backstreaming limit as a function of accel grid thickness.

Figure 19 shows how the crossover and perveance limits change as a function of screen grid thickness. All of the data reported regarding screen grid thickness was taken at an accel grid voltage of –750 V, as this was the voltage necessary to prevent electron backstreaming at the thinnest screen grid thickness of 1.31 mm/mm. Using all five data points in this figure, the sensitivities of the crossover and perveance limits to screen grid thickness were –1.41 and –0.27 respectively. If only the three data points surrounding the standard thickness of 3.94 mm/mm are used, the sensitivity of the crossover limit to screen grid thickness changes to –1.20, while the perveance limit sensitivity stays nearly the same at –0.25. The large change in the magnitude of the crossover and perveance limits in Fig. 19 was partly due to the fact that the relative change of screen grid thickness was large. For instance, the 6.56 mm/mm screen grid thickness was 67 % greater than the 3.94 mm/mm grid thickness.

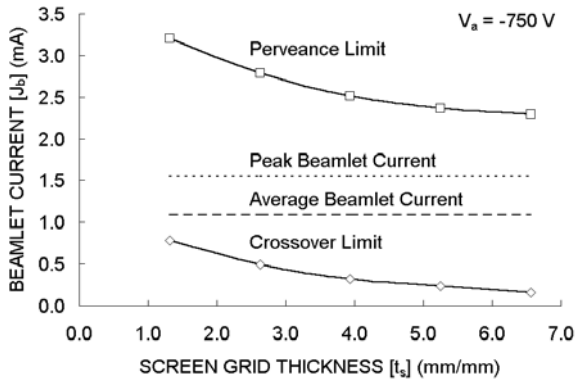

Fig. 19 Variation of the crossover and perveance limits with changing screen grid thickness.

Figure 20 shows the saddle point potential along the centerline of each ion beamlet as a function of beamlet current for all five screen grid thickness values. The shape of the saddle point potential curve changes considerably as the screen grid thickness is changed. The beamlet current with the least margin against electron backstreaming changed from 1.38 mA at a screen grid thickness of 1.31 mm/mm to 0.57 mA at a screen grid thickness of 6.56 mm/mm. Taking the maximum saddle point potentials from Fig. 20 and then considering the relationship found previously between saddle point voltage and accel grid voltage, the predicted backstreaming limit as a function of screen grid thickness is displayed in Fig. 21. Thus, the backstreaming limit was seen to vary nearly linearly with screen grid thickness.

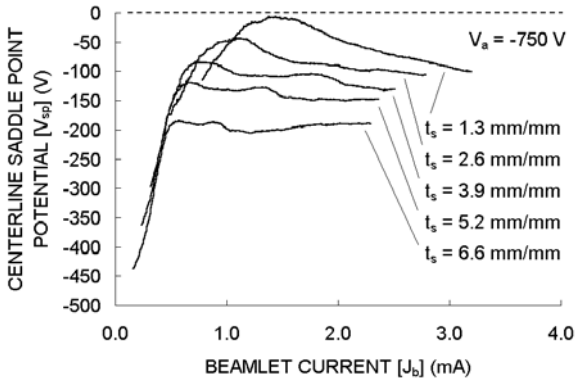

Fig. 20 Saddle point potential as a function of beamlet current for the five screen grid thickness values.

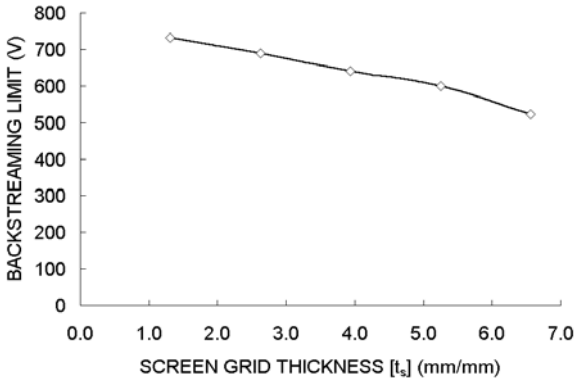

Fig. 21 Predicted backstreaming limit as a function of screen grid thickness.

As mentioned before, screen grid thickness, along with aperture center-to-center spacing, strongly affects the cross sectional shape of the ion beamlet and the screen grid transparency to ions. The physical transparency of the standard grid set is 68.6 %, which is calculated using a 5.20 mm/mm hole center-to-center spacing and a 5.25 mm/mm screen grid hole diameter. The shape of the sheath above each hole at a particular beamlet current can allow for a greater or lesser ion transparency than the physical transparency. Figure 22 shows the sheath shape at a beamlet current of 1.25 mA for screen grid thickness values of 1.31, 3.94, and 6.56 mm/mm. As screen grid thickness was increased, both the crossover and perveance limits decreased. The overall operating range, i.e. the difference of the crossover and perveance limits, decreased slightly, from 2.42 mA to 2.14 mA, as screen grid thickness was increased. Typically, a more dished sheath indicates a greater transparency to ions as more ions entering the edge of the hole are able to turn away from, instead of impinge upon, the screen grid.

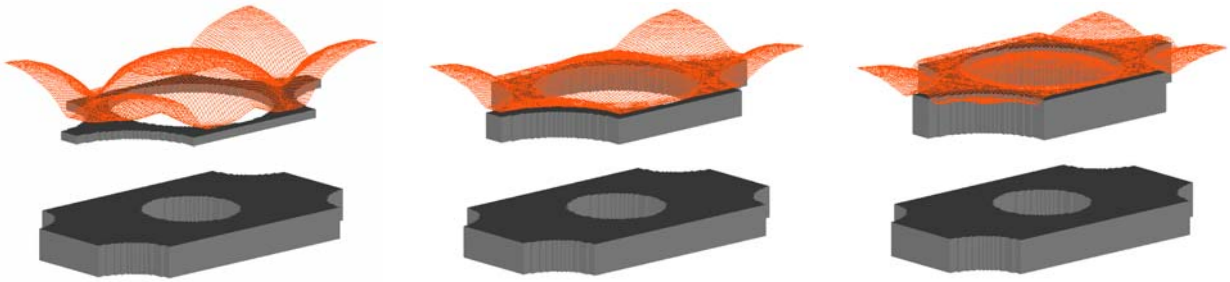

t_s = 1.31 mm/mm
ϕ = 87.0 %

t_s = 3.94 mm/mm
ϕ = 72.5 %

t_s = 6.56 mm/mm
ϕ = 57.2 %

Fig. 22 Sheath shape as a function of screen grid thickness at a beamlet current of 1.25 mA.

For the standard grid geometry at the average beamlet current of 1.09 mA, the ion transparency was calculated to be 74.1 %. Figure 23 shows the ion transparency as a function of screen grid thickness for beamlet currents of 1.0 mA, 1.5 mA, and 2.0 mA. These three beamlet currents are within the crossover and perveance limits at all five screen grid thickness values. The grid transparency to ions is seen to decrease nearly linearly with increasing grid thickness. At the 5.25 and 6.56 mm/mm screen grid thickness values, many of the apertures on the thruster grid set would be operating with ion transparencies lower than the physical transparency.

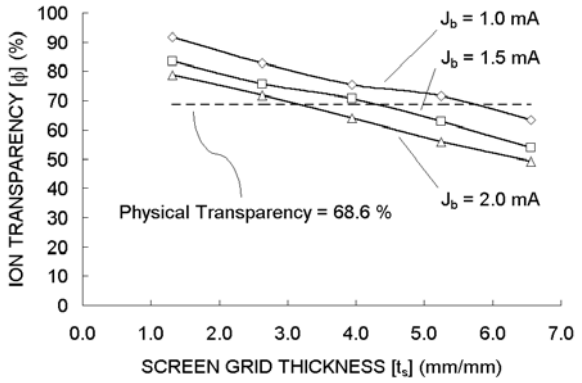

Fig. 23 Grid transparency to ions as a function of screen grid thickness for three beamlet currents.

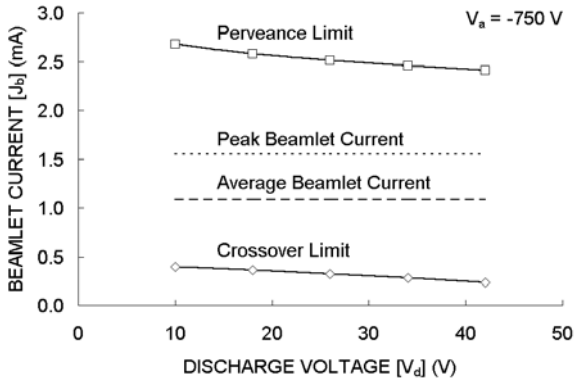

Fig. 24 Crossover and perveance limit as a function of discharge voltage.

Figure 24 shows the variation in the crossover and perveance limits as discharge voltage is varied from 10 to 42 V. The sensitivities of the crossover and perveance limits as a function of discharge voltage turned out to be –0.4 and –0.09 respectively. Thus, the crossover limit was a stronger function of discharge voltage than was the perveance limit.

In changing the discharge voltage, the net and accel grid voltages were held constant while the screen grid voltage was varied to maintain the same potential difference between the discharge and beam plasmas. For each 10 V rise in screen grid voltage (i.e., a 10 V decrease in discharge voltage), the backstreaming limit was seen to increase by about 5 V. For instance, the accel grid voltage needs to be about 13 V more negative to stop electrons from backstreaming at the 10 V discharge voltage case than at the 26 V discharge voltage case.

The variations in the crossover and perveance limits obtained when varying the accel grid hole diameter are shown in Fig. 25. All of the data in this figure were obtained at an accel grid voltage of –1050 V. The sensitivities of the crossover and perveance limits to accel grid hole diameter were found to be –1.73 and 0.97 respectively. The experimentally determined sensitivities, using slightly different grid geometry, to the crossover and perveance limits with respect to accel grid hole diameter were –1.44 and 0.63 respectively.[5] The trends in the crossover and perveance limits shown in Fig. 25 were expected. As accel grid hole diameter is increased, there is more open area for ions to go through and the operating range should be increased at both the crossover limit and perveance limit ends of the impingement limit curve.

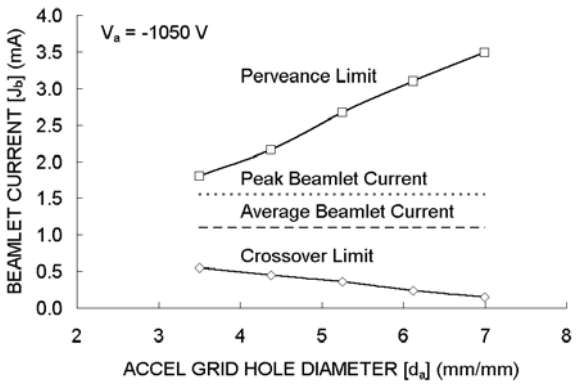

Fig. 25 Crossover and perveance limits as a function of accel grid hole diameter.

The diameter of the accel grid hole has a large affect on the required accel grid voltages to prevent electron backstreaming. Figure 26 shows how the saddle point potentials vary as a function of beamlet current for five accel grid hole diameters. The shape of the saddle point curve changes substantially with hole diameter. At the smallest diameter of 3.50 mm/mm, there is a peak on the curve at about 0.87 mA. However, at the largest diameter of 7.00 mm/mm, the saddle point potential continues to rise as beamlet current increases all the way to the perveance limit. Figure 27 shows the backstreaming limit as a function of accel grid hole diameter. At each hole diameter in this figure, several simulations at various beamlet currents and accel grid voltages were run to find the backstreaming limit.

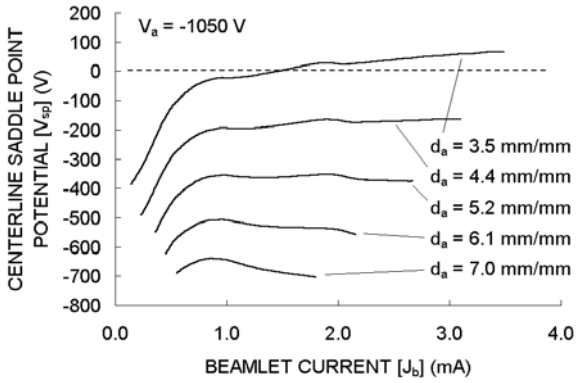

Fig. 26 Saddle point voltage variation with accel grid aperture diameter.

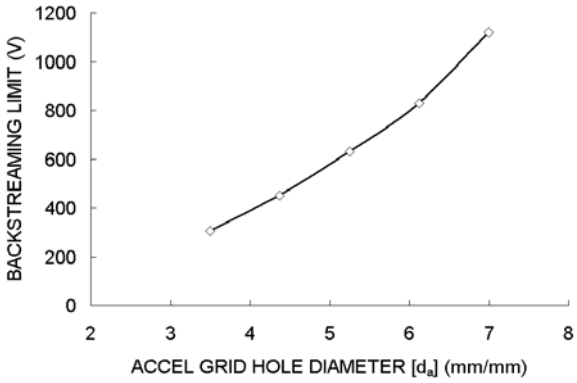

Fig. 27 Backstreaming limit as a function of accel grid aperture diameter.

HiPEP LIFE ASSESSMENT

All erosion simulations reported here were performed at a net accelerating voltage of 6700 V. The main parameters that were changed were beamlet current, accel grid voltage, and propellant utilization efficiency. The standard operating condition calls for a beam current of 3.5 A, and with roughly 3200 aperture pairs in the grid set, the average beamlet current is around 1.09 mA. The flatness parameter is expected to be near 0.7 (which was demonstrated in recent experiments conducted at NASA Glenn) and the propellant utilization efficiency around 0.9.

One of the main goals of the HiPEP thruster is to have a propellant throughput capability of 100 kg/kW or greater. The standard power is around 25 kW. With a propellant utilization efficiency of 0.92 and a beam current of 3.5 A, it is estimated that the thruster will have to operate for about 15 years (~131,400 hours) to reach the goal of 100 kg/kW. Accordingly, it will be the goal of any erosion simulation to reach about 135 khr of operation.

The two most probable reasons for the failure of the ion optics are both related to erosion of the accel grid. One failure mode is that of electron backstreaming. As discussed before, the accel grid should at all times be kept at a sufficiently negative voltage to prevent electrons from the downstream plasma from backstreaming upstream into the discharge chamber plasma. As was seen earlier, backstreaming voltage is a strong function of parameters like accel grid thickness and accel grid hole diameter. For this reason, the erosion of the inside of the accel grid hole, i.e. the barrel, tends to cause problems with electron backstreaming at end of life (EOL).

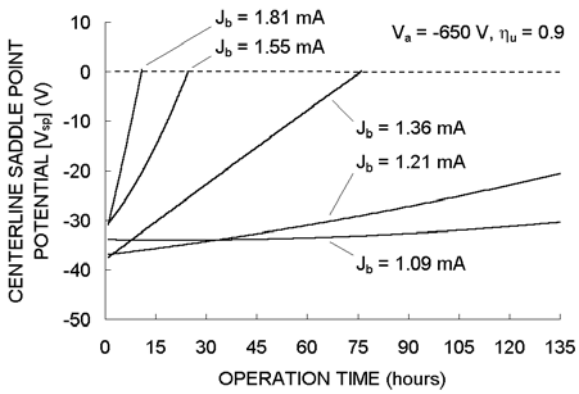

Fig. 28 Saddle point potential as a function of time. V_N = 6700 V, V_a = -650 V, η_u = 0.9.

The other failure mode occurs when the overall erosion of the accel grid becomes so great that the structural integrity of the accel grid is lost. In this case, for example, conducting material related to the erosion of the accel grid could possibly electrically short the screen and accel grid. The structural failure of the accel grid will be arbitrarily defined here as the point when the accel grid at any beamlet current is reduced to half of its initial mass.

At the standard operating condition, the accel grid applied voltage is –650 V. The margin against electron backstreaming at this accel voltage is predicted by the code to be small, about 25 V. Erosion calculations were performed at five beamlet currents at this condition. Beamlet currents of 1.09, 1.21, 1.36, 1.55, and 1.81 mA correspond to flatness parameters of 1.0, 0.9, 0.8, 0.7, and 0.6

respectively. Figure 28 shows the saddle point potential along the beamlet centerline as a function of operation time for these five beamlet currents. As can be seen in this figure, the apertures operating at 1.36, 1.55, and 1.81 mA are predicted to start backstreaming before 135 khr are reached. The mass loss from the accel grid for all of these cases was less than 10 % over the time that the saddle point potential was negative.

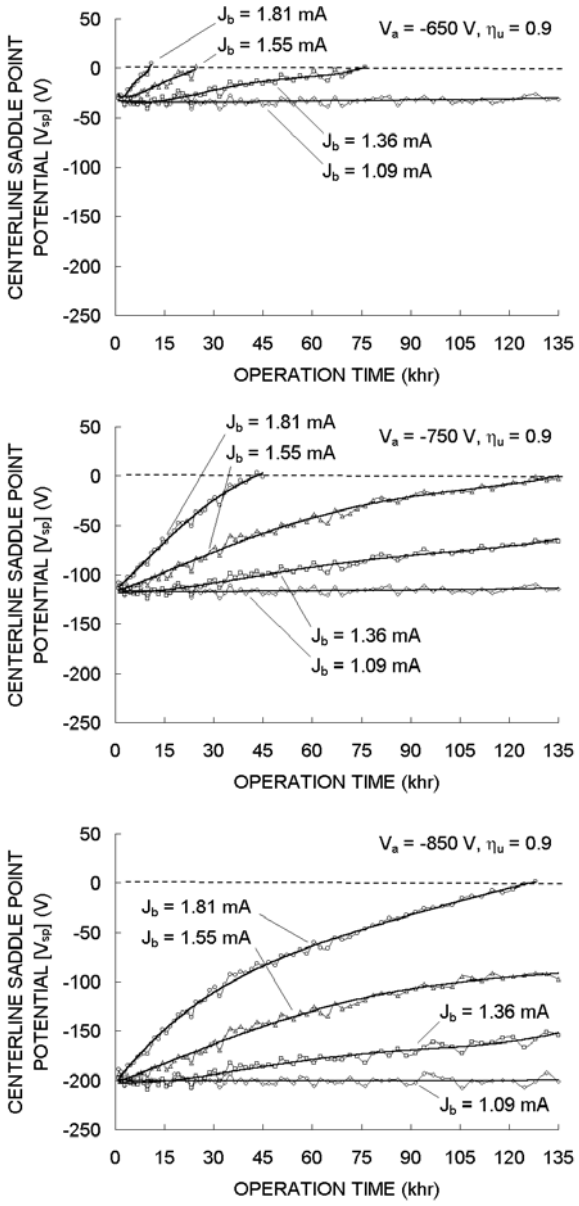

Fig. 29 Comparison of saddle point potential values as a function of time for three accel grid voltages.

A logical solution to the problem of electron backstreaming is to increase the accel grid voltage magnitude, either at the start of operation or during operation when the saddle point potential gets too positive. Figure 29 shows erosion cases for three accel grid voltages at beamlet currents of 1.09, 1.36, 1.55, and 1.81 mA. As accel grid voltage magnitude is increased from –650 to –850 V, the saddle point potential plots are basically shifted to more negative potentials. As was observed before, each 100 V increase in the accel grid voltage magnitude shifts the saddle point voltages more negative by about 85 V.

A consequence of increasing accel grid voltage is that the erosion rates from the accel grid generally become greater as a result of charge exchange ions striking the accel grid with more energy. Figure 30 shows the amount of mass that is remaining in the accel grid surrounding an aperture for four beamlet currents as a function of time at an accel voltage of –850 V. It can be seen in this figure that the greatest mass loss occurred at the 1.81 mA beamlet current, where about 20 % of the accel grid mass was lost just before 135 khr of operation, which is the point when electron backstreaming would start to occur.

Figure 31 shows a comparison of the mass loss from the accel grid at three accel grid voltages as a function of time for the 1.09 mA and 1.55 beamlet current cases. It can be seen in this figure that the increase in mass loss for every 100 V increase in the accel grid voltage magnitude was on the order of 0.7 to 0.8 % at 135 khr of operation for both beamlet currents. Overall, the increase in mass loss with increased accel grid voltage magnitude turned out to be small compared to the gain in the margin against electron backstreaming.

Figure 32 shows a progression of the erosion that takes place on the accel grid as a function of time at a beamlet current of 1.55 mA. At 0.0 khr of operation, there is of course no erosion from the accel grid. As time progresses, any cells in the simulation that are completely eroded away are colored in. The colors in this figure represent the axial distance of the erosion only. The red cells are cells at the upstream side of the accel grid that have been completely eroded away and the blue cells are cells near the downstream side of the accel grid that have been completely eroded away. Here, it can be seen that almost all of the erosion takes place on the accel grid barrel, and that it takes place mainly at the start of operation. At about 75 khr of operation, the barrel erosion has slowed and the accel grid hole diameter becomes more constant.

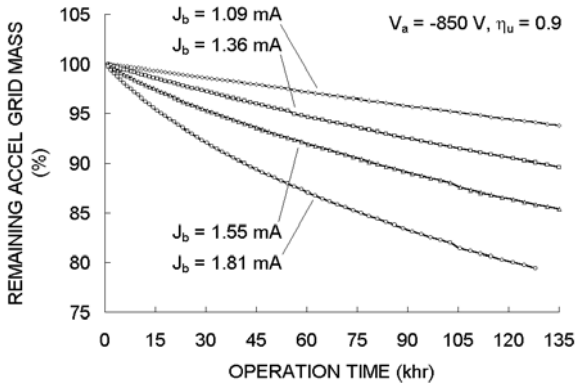

Fig. 30 Accel grid mass loss as a function of beamlet current at an accel grid voltage of –850 V.

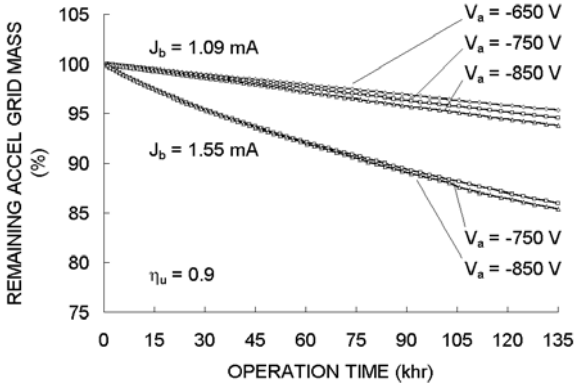

Fig. 31 Accel grid mass loss as a function of accel grid voltage at a beamlet current of 1.09 mA.

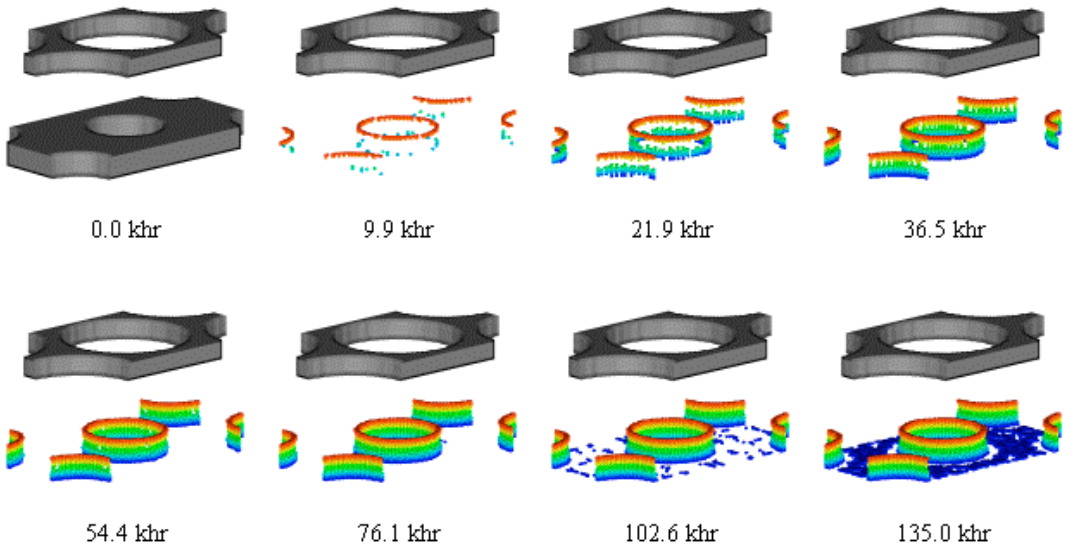

Fig. 32 Accel grid erosion at a beamlet current of 1.55 mA and accel grid voltage of –750 V.

Given that much of the erosion that takes place on the accel grid is from the accel grid barrel, it is understandable why the saddle point potential values are affected so greatly in relation to the overall accel grid mass loss. As was seen in Fig. 27, each 1.0 mm absolute, or 1.0 mm/mm relative, increase in accel grid aperture diameter increases the backstreaming limit by 200 V. Thus, even small increases in accel grid aperture diameter can have a large impact on the likelihood of electron backstreaming.

Charge exchange ions created between the screen and accel grids are what cause the erosion from the accel grid barrel. Figure 33 shows ion density, charge exchange ion production current, and the potential values within the beamlet operating at a current of 1.55 mA and accel grid voltage of –750 V. The amount of charge exchange ion production in each cell is proportional to the ion and neutral densities within the cell and the velocity of the ions going through the cell. The amount of energy that those charge exchange ions then strike the accel grid with is a function of the potential value where they were created. Charge exchange ions created at high potential values will have high energy when they strike the accel grid.

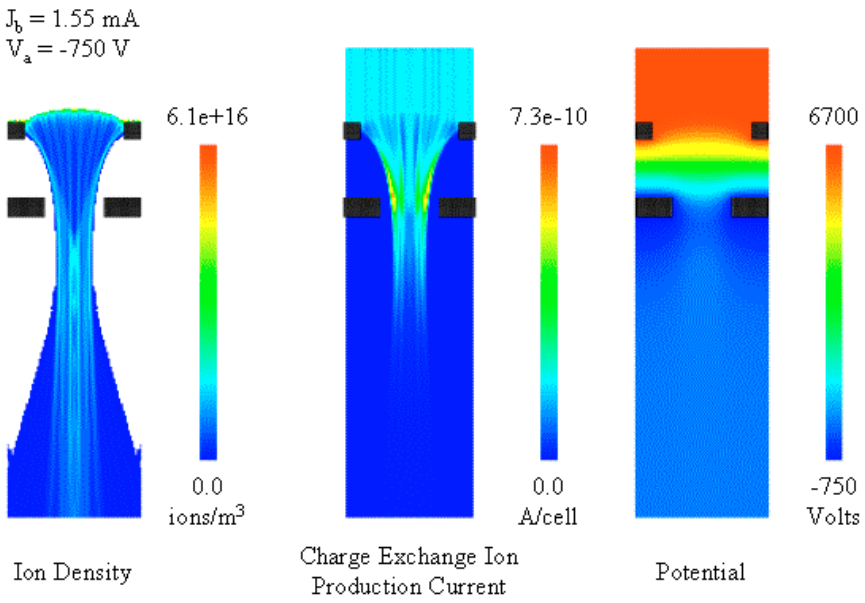

Fig. 33 The ion density, charge exchange ion production, and potential plots for a beamlet operating at a beamlet current of 1.55 mA and accel grid voltage of –750 V.

The charge exchange ions that are created within each cell will strike the downstream surface, screen grid, or accel grid. The simulation region in Fig. 34 is colored according to where the charge exchange ions end up going once they are created. The charge exchange ions that are created in the green region upstream of the screen grid are not tracked by the ffx code because they have the same trajectories as the beam ions that are injected into the upstream surface. In the green regions between the screen and accel grid and below the accel grid, no charge exchange ions are produced because there are no beam ions to interact with neutral particles. The charge exchange ions created in the blue regions in this figure end up being accelerated out the downstream surface of the simulation region.

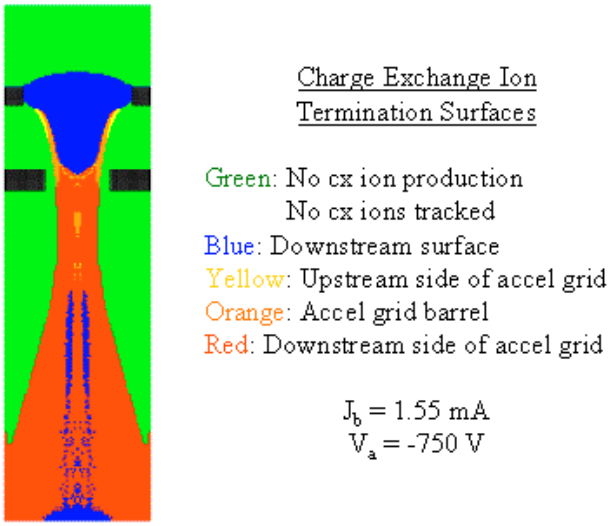

Fig. 34 Charge exchange ion termination points for a beamlet operating at a beamlet current of 1.55 mA and accel grid voltage of –750 V.

The charge exchange ions created in the yellow, orange, and red regions strike the accel grid. The charge exchange ions created in the yellow regions strike the upstream side of the accel grid, the orange regions strike the accel grid barrel between the upstream and downstream surfaces, and the red regions strike the downstream side of the accel grid.

Figure 35 shows the trajectories of charge exchange ions that originate from four planes within the region between the screen and accel grids. The charge exchange ions originating at the screen grid in (a) are accelerated out through the accel grid hole to the downstream surface. The charge exchange ions originating at the edges of the beamlet in (b), (c), and (d) strike the accel grid. Looking at the erosion patterns in Fig. 32 from about 9.9 to 36.5 khr, erosion first takes place from the upstream and downstream edges of the accel grid hole. Relating this erosion with the charge exchange ion trajectories in seen in Fig. 35, the erosion taking place at the upstream

edge of the accel grid hole is probably due to ions originating closer to the screen grid than the accel grid as in (b) and (c). The erosion on the downstream edge of the accel grid hole is probably more related to the charge exchange ions originating closer to the accel grid, as in (d), where the charge exchange production is higher although the potential is lower.

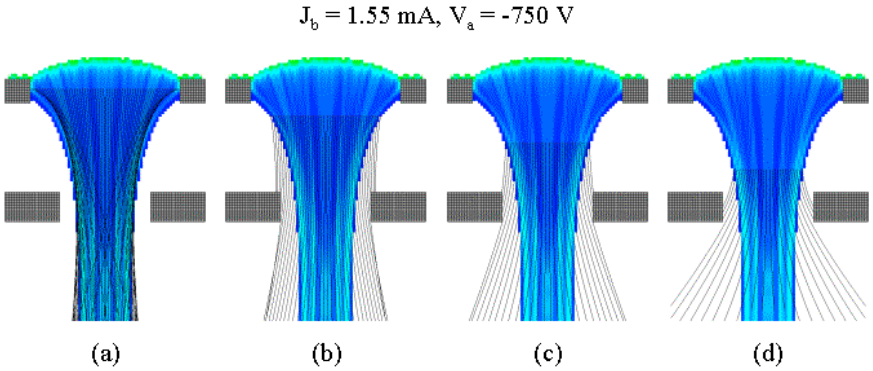

Fig. 35 Trajectories of charge exchange ions originating between the screen and accel grids at a beamlet current of 1.55 mA and accel grid voltage of –750 V.

The trajectories of charge exchange ions have a strong dependence on beamlet current. Ion density, which is directly related to beamlet current, affects both the potential values within the beamlet, and therefore the electric fields, and the amount of charge exchange ion production within each cell because of the relationship to beamlet shape. Figure 36 shows charge exchange ion termination points as a function of beamlet current. With increasing beamlet current, more ions originating between the screen and accel grids, where the potential is high, strike the upstream face and barrel of the accel grid.

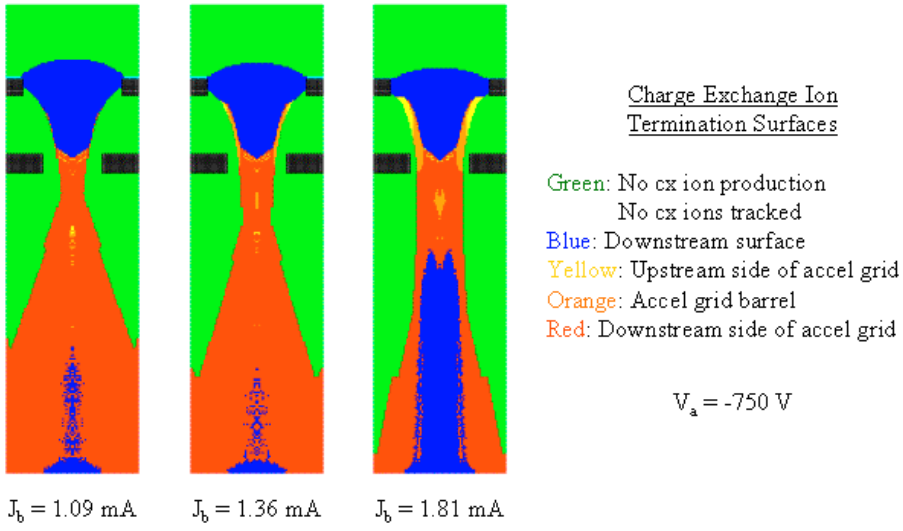

Fig. 36 Charge exchange ion termination surfaces at beamlet currents of 1.09, 1.36, and 1.81 mA.

All of the data reported above were run at a propellant utilization efficiency of 0.9. A study was done at an accel grid voltage of –850 V comparing the saddle point potential values and accel grid mass loss at propellant utilization efficiencies of 0.7, 0.8, and 0.9. Saddle point potential as a function of time is shown in Fig. 37 for beamlet currents of 1.09 and 1.55 mA and in Fig. 38 for beamlet currents of 1.36 and 1.81 mA. Reducing the propellant utilization efficiency shows a fairly large decrease in lifetime especially for the 1.81 mA beamlet current case.

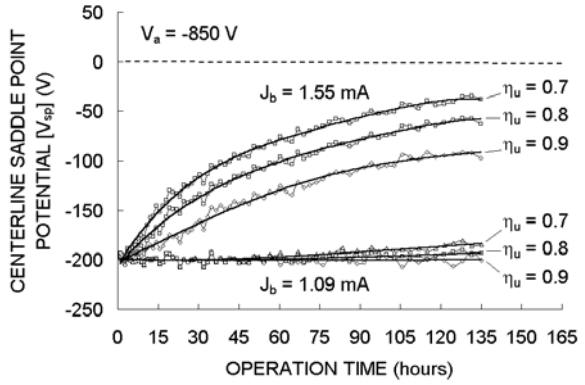

Fig. 37 Saddle point potential values for beamlet currents of 1.09 and 1.55 mA as a function of propellant utilization efficiency.

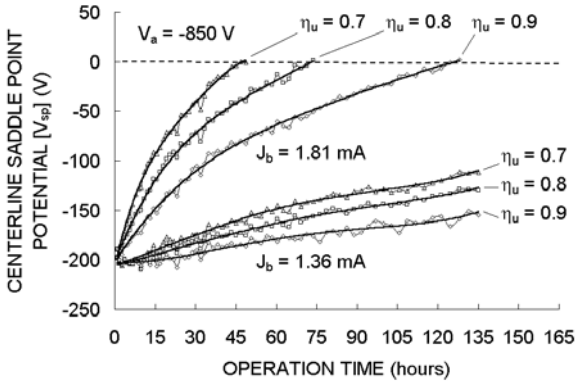

Fig. 38 Saddle point potential values for beamlet currents of 1.36 and 1.81 mA as a function of propellant utilization efficiency.

Figure 39 shows the remaining percentage of accel grid mass as a function of time at beamlet currents of 1.09 and 1.55 mA for the same three propellant utilization efficiencies of 0.7, 0.8, and 0.9. Similar to the large change in saddle point potential with utilization efficiency, the amount of mass loss from the accel grid also becomes significantly larger as propellant utilization is decreased. Figure 40 shows the remaining screen grid mass as a function of time. Here, instead of losing mass like the accel grid, the screen grid gains mass from material being eroded away from the accel grid and being deposited onto the screen grid. Over the total operational lifetime, the screen grid becomes more massive by about 6 % at the 1.55 mA beamlet current condition.

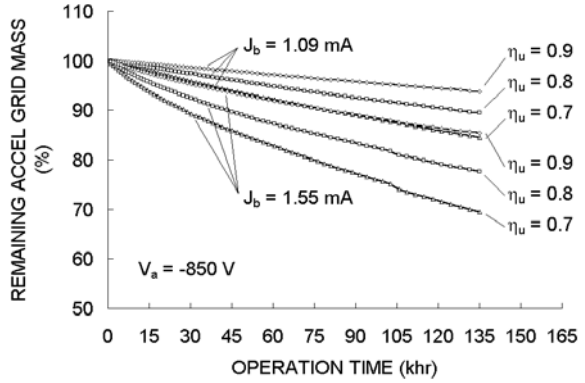

Fig. 39 Accel grid mass as a function of time and propellant utilization efficiency.

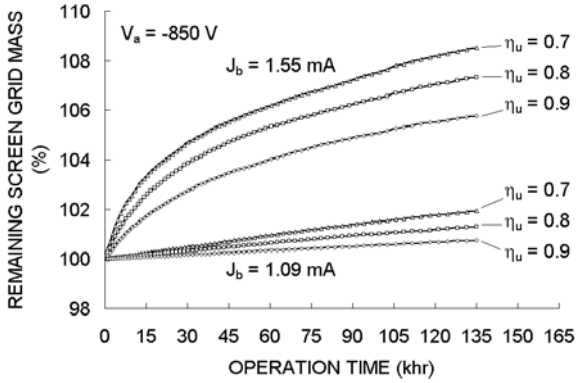

Fig. 40 Screen grid mass as a function of time and propellant utilization efficiency.

CONCLUSIONS

The ffx code was used to obtain trends in the effects that various design parameters have on the crossover, perveance, and backstreaming limits. Table 2 lists the results of these simulations. Erosion simulations that were performed for the standard net accelerating voltage case of 6700 V predict that much of the accel grid erosion will take place on the accel grid barrel region. The ffx code indicated a need for a slightly increased accel grid voltage to prevent electron backstreaming over the entire lifetime, approximately 15 years, of the thruster. Additionally, simulations at increased accel grid voltages and decreased propellant utilization efficiencies showed that the lifetime of the grid set was sufficient to obtain a propellant throughput capability of 100 kg/kW, one of the primary HiPEP thruster design goals.

Table 2. ffx code predicted sensitivities of various parameters on the crossover and perveance limits.

Parameter	Symbol	Units	Crossover Limit Sensitivity	Perveance Limit Sensitivity
Total Voltage - constant R	V_T	V	1.94	1.49
Total Voltage - constant V_N	V_T	V	2.02	1.53
Accel Grid Voltage	V_a	V	0.18	0.14
Effective Grid Spacing	ℓ_e	mm	-1.18	-2.05
Aperture Center-To-Center Spacing	ℓ_{cc}	mm	-0.59	0.05
Accel Grid Thickness	t_a	mm	0.52	-0.01
Screen Grid Thickness	t_s	mm	-1.20	-0.25
Discharge Voltage	V_d	V	-0.40	-0.09
Accel Grid Aperture Diameter	d_a	mm	-1.73	0.97

ACKNOWLEDGEMENTS

Results of this work were generated under the HiPEP Thruster Development Project being carried out in the On-Board Propulsion and Power Division at NASA Glenn Research Center, in support of NASA's Project Prometheus, with direction from Dr. John E. Foster, HiPEP Technical Program Manager, and Dr. George Williams, Senior Research Scientist. Financial support from NASA Glenn Research Center is gratefully acknowledged.

REFERENCES

1. Foster, J.E. et al. "An Overview of the High Power Electric Propulsion (HiPEP) Project." 40th Joint Propulsion Conference, AIAA-2004-3453, Fort Lauderdale, FL, July 2004.
2. Yamamura, Y., and Tawara, N. *Energy Dependence of Ion-Induced Sputtering Yields from Monatomic Solids at Normal Incidence*. Atomic Data and Nuclear Data Tables Vol. 62, Num. 2, March 1996, pp. 149-254.
3. Farnell, C.C., Williams, J.D., and Wilbur, P.J. "Numerical Simulation of Ion Thruster Optics." 28th International Electric Propulsion Conference, IEPC-03-073, Toulouse, France, March 2003.
4. Wilbur, P.J., Miller, J., Farnell, C.C., and Rawlin, V.K. "A Study of High Specific Impulse Ion Thruster Optics." 27th International Electric Propulsion Conference, IEPC-01-098, Pasadena, CA, 2001.
5. Williams, J.D., Farnell, C.C., Laufer, D.M., and Martinez, R.A. "HiPEP Ion Optics System Evaluation Using Gridlets." 40th Joint Propulsion Conference, AIAA-2004-3814, Fort Lauderdale, FL, July 2004